PAPER

Check for updates

Novel heterostructure Cu₂S/Ni₃S₂ coral-like nanoarrays on Ni foam to enhance hydrogen evolution reaction in alkaline media†

Yizhi Peng [ID] and Hanwei He*

Exploring efficient alternatives to precious noble metal catalysts is a challenge. Here, a new type of non-noble metal Cu₂S/Ni₃S₂ heterostructure nanosheet array is fabricated on 3D Ni foam. This electrocatalyst has excellent activity and durability to Hydrogen Evolution Reaction (HER) under alkaline conditions. The synergistic catalysis produced by the {$\bar{2}10$} and (034) crystal planes and the increase in charge transfer and the number of active sites caused by lattice defects greatly improve the electrocatalytic activity of Ni₃S₂. In the HER process, the Cu₂S/Ni₃S₂ interface increases the formation of S–H bonds, and Cu₂S promotes the transformation during the HER process into S-doped CuO, optimizing the adsorption capacity of S-doped sites for H. Among electrocatalysts made with different feed ratios, Cu₂S/Ni₃S₂/NF-3, for HER, only needs an overpotential of 50 mV to deliver a current density of 10 mA cm^{-2}. This work provides a promising non-noble metal electrocatalyst for water splitting under alkaline conditions.

1. Introduction

H₂, with its 142 MJ kg^{-1} energy density and nonpolluting reproducibility, is a sustainable energy source worthy of research.[1] The application of hydrogen energy urgently requires exploring cleaner, cheaper, and more efficient hydrogen production technology.[2] A viable clean hydrogen production technology is water splitting, but the overpotential requirements of the hydrogen evolution reaction (HER) and the oxygen evolution reaction (OER) limit the wide application. The slow HER kinetic process enormously limits the overall efficiency.[3] Platinum-based electrocatalysts are recognized as the top electrochemical HER catalysts. However, noble metal catalysts cannot be widely used due to practical factors. Commercially available traditional alkaline electrocatalysts are affordable but not sufficiently active,[4] such as stainless steel,[5] RANEY® nickel,[6] and nickel alloys.[7] Therefore, exploring catalysts that are effective for HER in abundant non-noble metal elements is urgent.

Owing to these practical problems, research has been carried out for decades to find substitutes for noble metals. Among them, high-performance nickel-based materials with excellent electrochemical performance and intrinsic electrocatalytic activity are expected to become the best candidates.[8-11] Among various nickel sulfides, Ni₃S₂ with inherent metallic advantages can be a suitable candidate for HER and OER catalysts.[12] As an effective catalyst active ingredient, Ni₃S₂ is widely used in

electrode materials for supercapacitors and lithium–sulfur batteries.[13] Miaomiao Tong[14] built special 3D Ni₃S₂ nano-rods@nanosheets, improved their adhesion properties, and exposed more active sites. However, Ni₃S₂ can still be modified in terms of increasing conductivity, improving catalytic activity, and exposing active sites.[15,16] Owing to the inevitable sulfur vacancies in Ni₃S₂, the regulation of its surface electronic structure has become a way to improve catalytic activity. Metallic element doping is a feasible solution. It can adjust the adsorption/desorption energy, expand the effective surface area, regulate the electronic structure, and exert a synergistic role between ions.[17-19] Relevant literature has reported that Fe,[20] Co,[21] Zn,[22] and Mo[23] doping in Ni₃S₂ improves HER or OER performance. However, Cu-doped high-activity Ni₃S₂ catalyst with a great HER performance has rarely been reported. Cu, as a doping element, does have a good effect. Several researchers doped Cu as catalytic materials. Zhang et al.[24] reported that the charge transfer ability and surface area of Cu-doped Fe–Co oxide have been greatly improved. Co/Cu-modified NiO designed by Guo, ZG et al.[25] proved that Cu doping can activate Ni sites at a low overpotential, thereby increasing conductivity and accelerating charge transfer. Until now, studies have focused on the use of doped modified substrate materials. For example, the recent report of Du's group about Cu doped Ni₃S₂ has an overpotential of 91 mV.[26] However, the intrinsic catalytic activity of each substance is different, and it is a novel idea to improve the catalytic activity by constructing a heterostructure. There are few reports on the heterostructure of Cu₂S and Ni₃S₂, which is a direction worth studying. We used the activity of Cu₂S to construct a heterostructure Cu₂S/Ni₃S₂ greatly improved the catalytic activity of Ni₃S₂ for hydrogen evolution.

Powder Metallurgy Research Institute, Central South University, Changsha, 410083, China. E-mail: hehanwei@csu.edu.cn

Based on the above viewpoints, a two-step hydrothermal method was designed to successfully grow Cu_2S/Ni_3S_2 with a stable and regular morphology heterostructure on nickel foam. In the first step, the precursor (Cu–Ni layered double hydroxide [LDH]) of the composite structure of nanosheets and nanowires is prepared by changing the feed ratio and reaction conditions. In the second step, a sulfide ion exchange is used to obtain the target sample ($Cu_2S/Ni_3S_2/NF$). The synergistic effect between Cu_2S and Ni_3S_2 of heterostructure makes the material obtain excellent HER performance. $Cu_2S/Ni_3S_2/NF$-3 to achieve a current density of 10 mA cm^{-2} only needs an overpotential of 50 mV, which is much lower than the reported Cu doped Ni_3S_2 and Ni–S–Cu systems.[26] The number of active sites calculated by the turnover frequency (TOF) is 3.568×10^{-4} mol. Moreover, the actual surface area of $Cu_2S/Ni_3S_2/NF$-3 is about 2.2 times that of Ni_3S_2/NF. The high electrocatalytic performance of $Cu_2S/Ni_3S_2/NF$ is mainly manifested in the following aspects: 1. After vulcanization, the surface of the layer structure is "coral-like," exposing abundant active sites and allowing the active ingredients to be in close contact with the electrolyte. 2. The combination of Cu_2S and Ni_3S_2, Cu_2S is converted into S-doped CuO during the HER process, where CuO introduces a defect level near the Fermi level, accelerates charge transfer and improves intrinsic conductivity.[27] 3. The high conductivity of Ni_3S_2 provides a fast charge transfer and promotes the electrocatalytic reaction of the catalyst. 4. High-index {$\bar{2}10$} of Ni_3S_2 and exposed (034) crystal plane of Cu_2S improve electrocatalytic performance.

2. Experimental section

2.1 Experimental materials preparation

In this experiment, chemicals include ionized water (>18.25 mΩ cm^{-1}, Millipore), and $CuCl_2 \cdot 2H_2O$, $NiCl_2 \cdot 6H_2O$, CH_4N_2O, NH_4F, Na_2S, all purchased from Sinopharm Chemical Reagent Co., Ltd. The nickel foam (NF) used in all experiment were obtained from Kunshan Desco Electronics Co., Ltd. (Suzhou, China) and the density of NF was 350 g m^{-2}.

2.1.1 Fabricating Ni–Cu LDH nanosheet array on NF. First, $CuCl_2 \cdot 2H_2O$ and $NiCl_2 \cdot 6H_2O$ were dissolved in deionized

water(70 mL) at different molar ratios (the specific feed ratio and the corresponding serial number are shown in Table 1), 10 mmol CH_4N_2O and 4 mmol NH_4F were add in above solution. Then the precursor solution, stirred for 10 minutes, was transferred into a 100 mL Teflon-line stainless autoclave. The prepared clean NF (2 × 5 cm) was immersed in it, then reacted at 120 °C for 6 h. After cooling, the obtained Ni–Cu LDH/NF was washed and then placed at 60 °C to dry overnight in a vacuum oven. Fig. 1 shows the schematic diagram of preparation of $Cu_2S/Ni_3S_2/NF$.

2.1.2 Ni–Cu LDH sulfide to Cu_2S/Ni_3S_2. Prepared 0.2mol L^{-1} Na_2S solution and dried NiCu-LDH were put into Teflon-line stainless autoclave. After reacting at 100 °C for 8 h, the black $Cu_2S/Ni_3S_2/NF$ was obtained. After the $Cu_2S/Ni_3S_2/NF$ is washed and dried, the subsequent characterization and performance can be performed.

2.2 Preparation for material characterizations and electrochemical measurements

The X-ray diffraction (XRD) of Ni–Cu LDH and Cu_2S/Ni_3S_2 was measured using a PANalytical Empyren equipment at 45 kV and 40 mA with a Cu target. The scanning electron microscopy (SEM) images of Ni–Cu LDH and Cu_2S/Ni_3S_2 were from Zeiss Sigma 500. Energy dispersive spectroscopy (EDS) analyses were recorded by FEI Talos 200s. The valence states of the elements on the electrode surface were obtained by an ESCALAB 250Xi X-ray photon spectrometer (XPS). Transmission electron microscopy (TEM), selected area electron diffraction (SAED), high-resolution TEM (HRTEM), and scanning TEM were all obtained by using a JEM2100F microscope.

All electrochemical tests use CHI660B electrochemical workstation. A three-electrode system consisting of graphite, saturated calomel electrodes (SCE, KCl saturated) and the sample to be tested was made up in 1 M KOH at 25 °C. The potentials measured in the experiment has been calibrated, and the potential (vs. SCE) was converted into a reversible hydrogen electrode (RHE) through the Nernst equation:[28] $E_{vs. RHE} = E_{vs. SCE} + 0.242$ V $+ 0.059$ pH. The polarization curves were corrected by the equation:[29] $E_{corrected} = E_{vs. RHE} - iR$ linear sweep voltammetry (LSV), cyclic voltammetry (CV), electrochemical impedance spectroscopy (EIS) and continuous CV cycles were used to evaluate the electrocatalytic performance of the catalyst.

3. Experimental results

3.1 Cu_2S/Ni_3S_2 structure analysis

NF with 3D conductive network structure and macropores was used as a base material for electrocatalyst growth. After the two-step hydrothermal reaction mentioned above, the silver white

Table 1 Different feed ratios and corresponding numbers

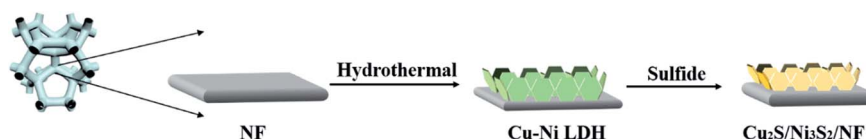| $CuCl_2 \cdot 2H_2O$	$NiCl_2 \cdot 6H_2O$	Corresponding Cu–Ni LDH
2 mmol	2 mmol	Cu–Ni LDH/NF-0
2 mmol	4 mmol	Cu–Ni LDH/NF-1
2 mmol	8 mmol	Cu–Ni LDH/NF-2
2 mmol	18 mmol	Cu–Ni LDH/NF-3
2 mmol	24 mmol	Cu–Ni LDH/NF-4

Fig. 1 Schematic diagram of preparation of $Cu_2S/Ni_3S_2/NF$.

NF changed to brick red (the NiCu LDH precursor) and then black (Cu$_2$S/Ni$_3$S$_2$/NF). The SEM images in Fig. 2(a)–(f) can visually present the microscopic morphology of the sample. Fig. 2(a)–(c) show the SEM images of NiCu LDH. NiCu LDH is uniformly anchored on the NF substrate in a sheet-like manner. After further increasing the magnification, "nano fluff" was evenly distributed on the nanosheets. Compared with NiCu LDH, the SEM images of Cu$_2$S/Ni$_3$S$_2$/NF did not change significantly, as shown Fig. 3(d)–(f), indicating that the required LDH layered structure can exist stably. After vulcanization, the "nano fluff" is transformed into a "coral" with a rough surface, exposing more active sites. The SEM picture of Cu$_2$S/Ni$_3$S$_2$/NF after 58 h chronopotentiometry test is placed in the support information. As shown in Fig. S1,† some cracks appeared on Cu$_2$S/Ni$_3$S$_2$ layer after the test. And the original thin nanosheets are transformed into a stacked coral layer. This transition from

"nano fluff" to "rough coral" increases the specific surface area and helps improve electrocatalytic activity.

Furthermore, Fig. 2(g) shows the XRD pattern of Ni$_3$S$_2$/NF and Cu$_2$S/Ni$_3$S$_2$/NF. Both XRD spectra have the same three strong peaks, based foam nickel (PDF #70-1849). The diffraction peaks of both at $2\theta = 21.75°$, $31.10°$, $37.78°$, $49.73°$, and $55.16°$ correspond to Ni$_3$S$_2$ (PDF #44-1418) (101), (110), (003), (113), and (122) crystal planes, respectively. Obviously, the characteristic peak of Cu$_2$S (PDF #33-0490) appeared in the XRD spectrum (indicated by the orange line) after Cu was added. The XRD spectrum qualitatively showed the existence of Cu$_2$S/Ni$_3$S$_2$. EDS confirms that Ni, Cu, and S are present in Cu$_2$S/Ni$_3$S$_2$/NF sample, and their atomic ratio is close to the feed ratio. The Cu$_2$S/Ni$_3$S$_2$/NF after 58 h chronopotentiometry test was characterized by XRD. As shown in the ESI Fig. S2,† after the 58 h stability test, the XRD spectrum of Cu$_2$S/Ni$_3$S$_2$/NF showed a CuO
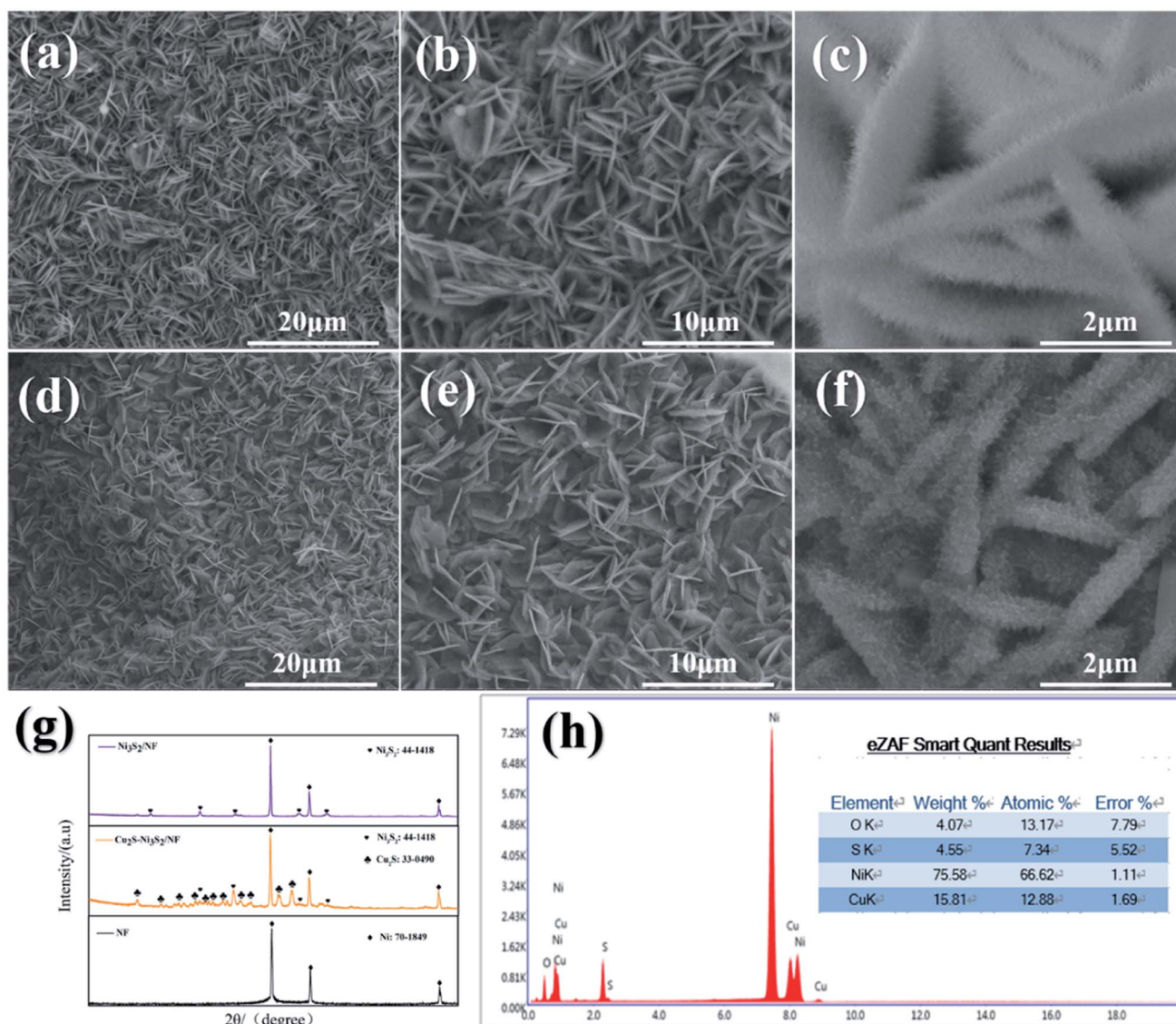
Fig. 2 (a–c) SEM image of NiCu LDH-3, (d–f) SEM image of Cu$_2$S/Ni$_3$S$_2$/NF-3, (g) XRD pattern of Ni$_3$S$_2$/NF, Cu$_2$S/Ni$_3$S$_2$/NF and NF, (h) EDS image of Cu$_2$S/Ni$_3$S$_2$/NF.
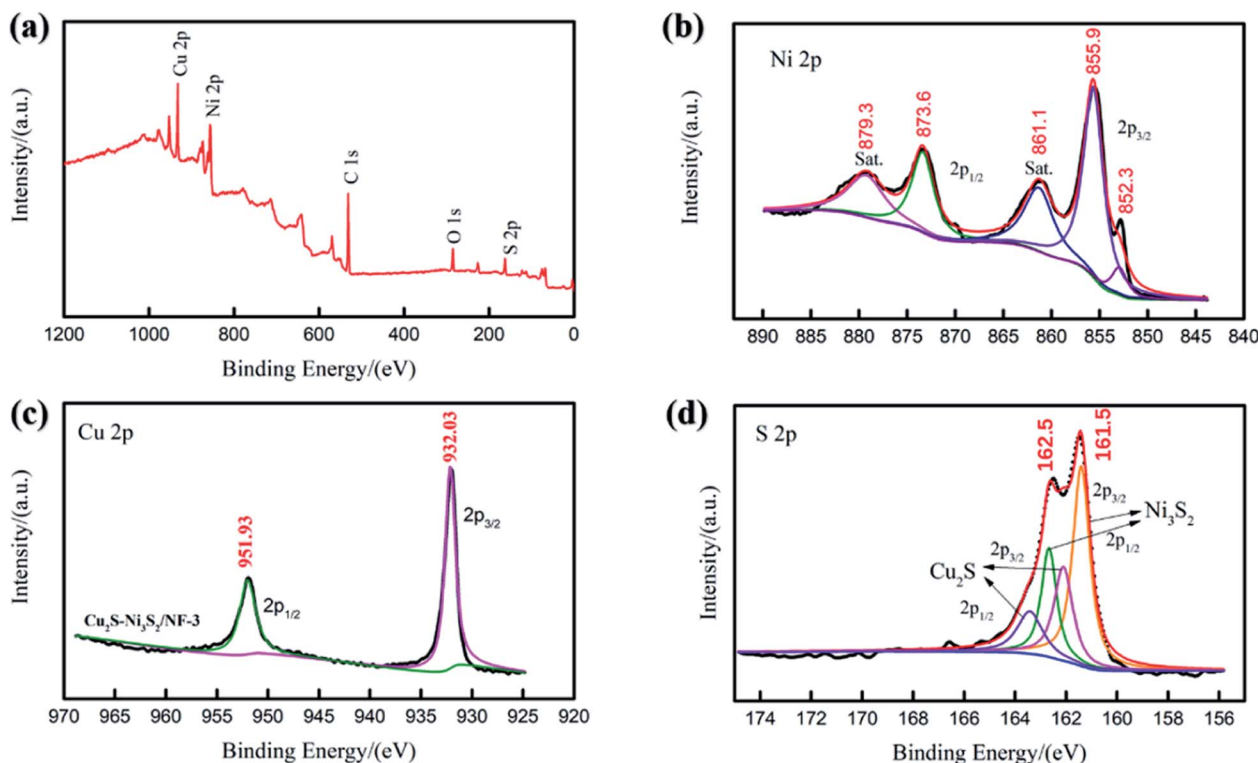
Fig. 3 (a) XPS survey spectrum for Cu_2S/Ni_3S_2. XPS spectra of Cu_2S/Ni_3S_2 in the (b) Ni 2p, (c) Cu 2p and (d) S 2p regions.

peak (PDF #89-5899) that had not appeared before the test. The diffraction peaks at $2\theta = 35.6°$, $38.8°$, and $48.7°$ correspond to CuO (-111), (111), and (-202) crystal planes, respectively. The intensity of the Cu_2S peak weakened, indicating that Cu_2S was partially converted to CuO.

In addition, the element composition of $Cu_2S/Ni_3S_2/NF$-3 can be obtained by XPS. The overall XPS spectrum of $Cu_2S/Ni_3S_2/NF$-3 is shown in Fig. 3(a), where Ni, Cu, and S are present. Fig. 3(b) shows the XPS spectrum of the Ni 2p region, where the intensities of the Ni $2p_{1/2}$ and Ni $2p_{3/2}$ peaks are 855.48 eV and 873.23 eV, respectively, indicating that Ni exists in the form of Ni_3S_2.[30] The peaks of 879.2 and 860.8 eV are the concomitant satellites.[31,32] The small peak on the far right (852.8 eV) is a typical metal nickel sulfide or metal nickel peak.[33] In the XPS spectrum of Cu 2p region shown in Fig. 3(c), 932.03 eV is the peak of Cu $2p_{3/2}$ in Cu_2S, and 951.93 eV is the peak of Cu $2p_{1/2}$.[34] The last picture in Fig. 3(d) is the XPS spectrum of S 2p, where 162.48 and 161.48 eV are attributed to S $2p_{1/2}$ and $2p_{3/2}$ in Ni_3S_2, respectively.[35] And 162.25 eV is attributed to S $2p_{3/2}$ in Cu_2S. All XPS spectra fully prove that the synthesized sample is Cu_2S/Ni_3S_2. After 58 h chronopotentiometry test, the XPS spectra of the electrode is placed in the ESI Fig. S3.† In Fig. S3(b)† shows that Ni $2p_{3/2}$ and Ni $2p_{1/2}$ of Ni_3S_2 are the main strong peaks, which can match the conclusion of XRD (Fig. S2†). Moreover, in Fig. S3(b).† The Cu 2p spectra (Fig. S3(c)†) shows Cu^+ and Cu^{2+} peaks. Among them, the Cu $2p_{3/2}$ and Cu $2p_{1/2}$ match with the Cu_2S and the strong Cu^{2+} satellite match with the CuO detected by XRD (Fig. S2†). Compared with the original XPS spectra, the intensity of S 2p (Fig. S3(d)†) is reduced after the chronopotentiometry test. We suspected that the heterostructure

Cu_2S/Ni_3S_2 catalyst is converted to sulfur-doped CuO in this process. It is reported that the ΔG_{H*} of sulfur-doped CuO is lower than that of pure CuO.[36] The heterostructure between Cu_2S/Ni_3S_2 promotes interface electron transfer. The Ni sites at the Cu_2S/Ni_3S_2 interface interact with O in water molecules to adsorb water molecules on the surface. After that, the water molecules adsorbed on the Ni site interact with hydrogen bonds or form S–H bonds, which accelerate the adsorption and dissociation of water and increase the speed of the Volmer step.[37–39] It is reported that S optimizes the free energy of H* ($\Delta EH*$) adsorption of CuO, and the O site of CuO near the S-doped site increased the H adsorption capacity.[40]

Fig. 4(a) clearly shows the TEM image of $Cu_2S/Ni_3S_2/NF$ layer structure stacked on top of one another. The SAED pattern of $Cu_2S/Ni_3S_2/NF$ in Fig. 4(b) shows typical polycrystalline diffraction rings. These calibrated diffraction rings can correspond well to the peak of the XRD spectrum. Comparing with the PDF card confirmed it to be Ni_3S_2. The diffraction ring of the (034) crystal planes of Cu_2S can also be observed, which corresponds to the strong peak appearing after Cu doping in the XRD spectrum. The exposed (034) crystal planes of Cu_2S is beneficial for the improvement of the HER performance of the catalyst. The HRTEM lattice fringe image of Cu_2S/Ni_3S_2 is in Fig. 4(c). The crystal planes with interplanar spacings of 0.287, 0.234, and 0.237 nm correspond to the (110), (021), and (003) crystal planes of Ni_3S_2 (PDF#44-1418), respectively. The exposed crystal surface of the catalyst has an important influence on its catalytic performance. The angle between the two (110) is 60°, indicating that the thermodynamically stable {001} crystal planes is exposed. The angle between (003) and (021) is about 70.5°, then

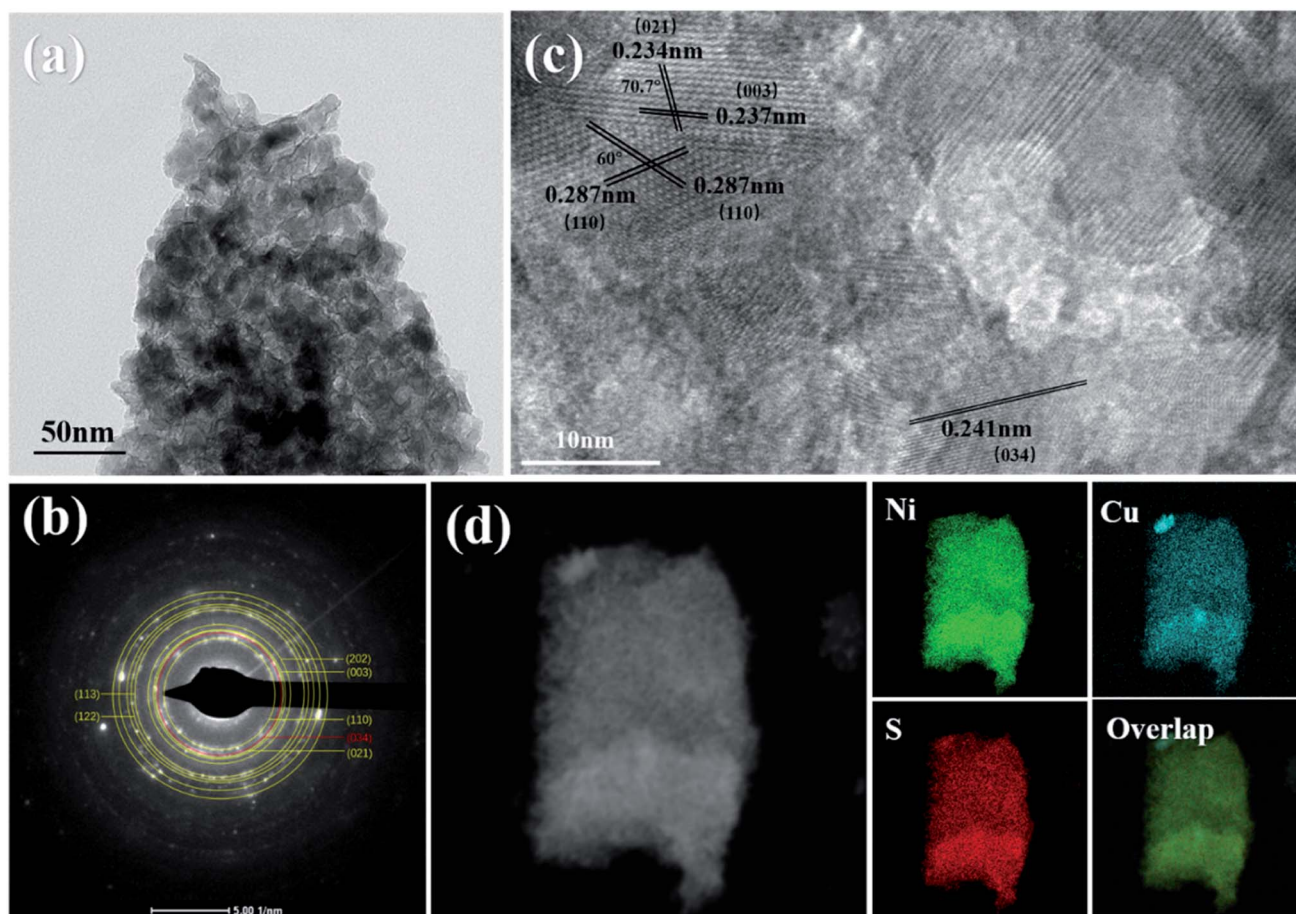**Fig. 4** (a) TEM image of Cu_2S/Ni_3S_2 layer structure, (b) SAED pattern and (c) HRTEM image of Cu_2S/Ni_3S_2, (d) mapping of Ni, Cu, S and overlap images of Cu_2S/Ni_3S_2 nanosheet.

high-index $\{\bar{2}10\}$ is exposed.[41] Research by Liang-Liang Feng *et al.*[41] showed that the synergistic catalysis produced by the nanosheet array and the exposed $\{\bar{2}10\}$ high-index facets help improve electrocatalytic performance. Numerous disordered defects and the exposed (034) crystal planes of Cu_2S can also be observed in the HRTEM image, indicating that the exposed active sites and electrical conductivity can be increased.[42] Moreover, the mapping of Cu_2S/Ni_3S_2 nanosheet in Fig. 4(d) reflects that Ni, S, and Cu are evenly distributed on the nanosheets, which is conducive to the uniform dispersion of active sites.

3.2 Catalyst electrochemical performance analysis

3.2.1 Catalyst HER performance.
The LSV of Pt/C, $Ni_3S_2/$NF, and $Cu_2S/Ni_3S_2/$NF-*x* (*x* represents various feed ratios) was

Table 3 Comparison of the electrocatalysts performance of $Cu_2S/Ni_3S_2/$NF and other Ni_3S_2

Catalysts	Electrolyte Solution	Overpotential (η_{10})
$Cu_2S/Ni_3S_2/$NF-3	1 M KOH	50 mV
$S-v-Ni_3S_2-xP_{x-4}$ (ref. 44)	1 M KOH	89 mV
Mo-doped Ni_3S_2 (ref. 45)	1 M KOH	90 mV
V-doped $Ni_3S_2/$NiS[46]	1 M KOH	85 mV
$CoNi_2S_4/Ni_3S_2$@NF[47]	1 M KOH	171 mV

Table 2 Comparison of overpotential of different samples

Catalysts	Current density $(j\ \text{mA cm}^{-2})$	Overpotential (η/mV)
Pt/C	10	31
$Ni_3S_2/$NF	10	180
$Cu_2S/Ni_3S_2/$NF-0	10	182
$Cu_2S/Ni_3S_2/$NF-1	10	159
$Cu_2S/Ni_3S_2/$NF-2	10	122
$Cu_2S/Ni_3S_2/$NF-3	10	50
$Cu_2S/Ni_3S_2/$NF-4	10	134

Table 4 Number of active sites of $Cu_2S/Ni_3S_2/$NF-*x* and $Ni_3S_2/$NF

Catalysts	Number of active sites $(\times 10^{-4}\ \text{mol})$
$Ni_3S_2/$NF	1.625
$Cu_2S/Ni_3S_2/$NF-2	2.639
$Cu_2S/Ni_3S_2/$NF-3	3.568
$Cu_2S/Ni_3S_2/$NF-4	3.533
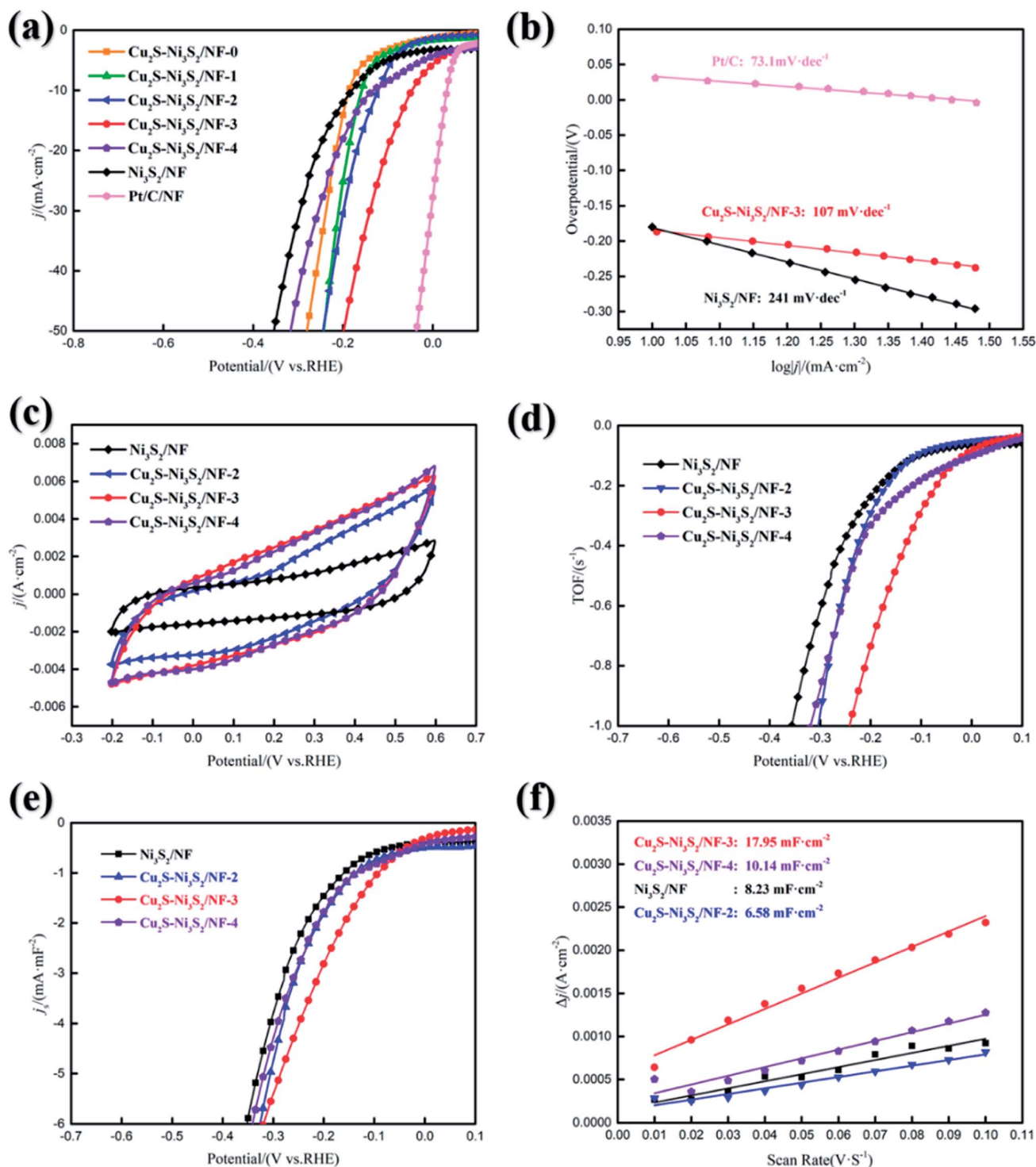
Fig. 5 (a) *iR*-Corrected linear sweep voltammetry curves of Ni_3S_2/NF and Cu_2S/Ni_3S_2/NF-*x* (*x* represents various feed ratios) for HER in 1 M KOH at 5 mV s^{-1}, (b) Tafel plots of Ni_3S_2/NF, Pt/C and Cu_2S/Ni_3S_2/NF-3, (c) CVs of Ni_3S_2/NF and Cu_2S/Ni_3S_2/NF-*x* at pH = 7 at the scan rate of 50 mV s^{-1}, (d) TOF curves of Ni_3S_2/NF and Cu_2S/Ni_3S_2/NF-*x*, (e) polarization curves of Ni_3S_2/NF and Cu_2S/Ni_3S_2/NF-*x* normalized by the ECSA, (f) measured capacitive currents plotted as a function of scan rate.

evaluated in 1 M KOH solution. Comparing the polarization curves clearly shows that Pt/C has the best HER performance (η_{10} = 31 mV), whereas Ni_3S_2/NF requires 180 mV. The Cu_2S/Ni_3S_2/NF-3 curve, which is closest to Pt/C curve, requires an

overpotential of 50 mV at 10 mA cm^{-2}. The overpotentials of five samples are shown in Table 2. Compared with Ni_3S_2/NF, the HER performance of Cu_2S/Ni_3S_2/NF is indeed improved much. However, experiments have shown that the amount of Cu

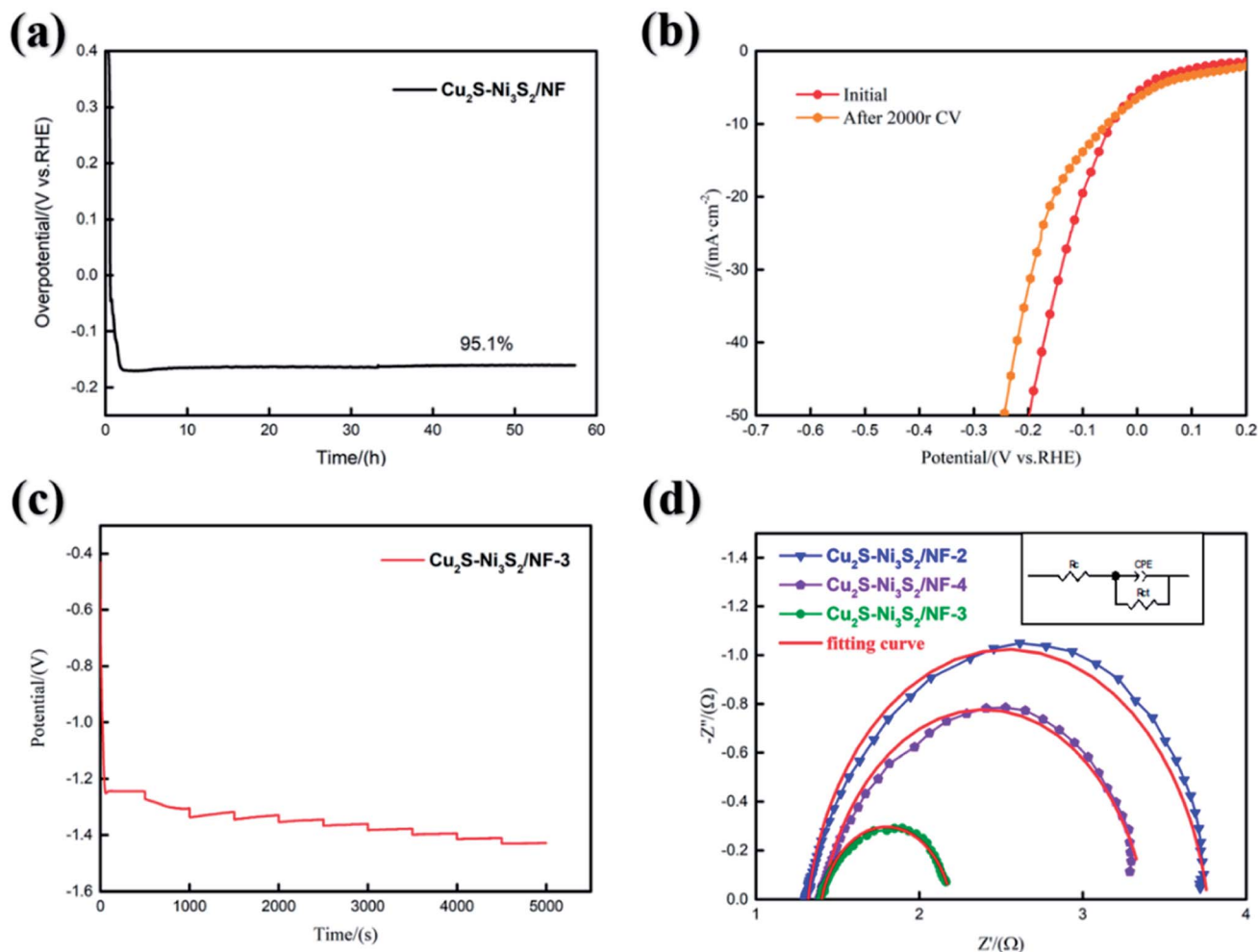Fig. 6 (a) The chronopotentiometry curve of Cu$_2$S/Ni$_3$S$_2$/NF at constant current density of 10 mA cm^{-2}. (b) The polarization curves of Cu$_2$S/Ni$_3$S$_2$/NF-3 before and after 2000 CV cycles. (c) Stability test of Cu$_2$S/Ni$_3$S$_2$/NF-3 carried out at multiple currents. (d) Impedance Nyquist plots of Cu$_2$S/Ni$_3$S$_2$/NF-2, Cu$_2$S/Ni$_3$S$_2$/NF-3 and Cu$_2$S/Ni$_3$S$_2$/NF-4.

cannot be too much, which is consistent with Byung Keun Kim's report[43] that excessive Cu will increase the internal stress and cause the coating to fall off, thereby reducing catalytic performance. Cu$_2$S/Ni$_3$S$_2$/NF was also compared with the results of other scientific researchers. Detailed data can be found in Table 3.

In alkaline solution, HER follows Volmer–Tafel or Volmer–Heyrovsky mechanism.[48] They all consist of three steps: 1. Discharge (H$_2$O + e$^-$ → H* + OH$^-$, Volmer reaction) 2. Electrochemical desorption (H$_2$O + H* + e$^-$ → H$_2$ + OH$^-$, Heyrovsky reaction) and 3. Recombination (2H* → H$_2$, Tafel reaction). The calculated Tafel slope of Cu$_2$S/Ni$_3$S$_2$/NF-3 is 107 mV dec^{-1} (lower than 120 mV dec^{-1}), indicating that hydrogen evolution is mainly limited by the Volmer reaction and follows the Volmer–Heyrovsky mechanism. The Tafel slope of Cu$_2$S/Ni$_3$S$_2$/NF-3 is clearly much smaller than that of Ni$_3$S$_2$/NF, indicating that Cu$_2$S/Ni$_3$S$_2$/NF-3 catalytic reaction kinetics is faster in an alkaline medium, and the catalytic activity of HER is better.[49]

Turnover frequency (TOF) can be used to reflect intrinsic activity.[50] First, CV curves were measured in a ph = 7 phosphate

buffer saline solution at a scan rate of 50 mV s^{-1} and a voltage range of −0.2–0.6 V. Then, the number of active sites was calculated from the method reported by Merki.[51] In Table 4, the active sites loaded on the Cu$_2$S/Ni$_3$S$_2$/NF-3 surface is 3.568 × 10^{-4} mol, which is more than Ni$_3$S$_2$/NF (1.625 × 10^{-4} mol). This result may be related to the coral-like surface on the nanosheet shown in the SEM image. This specific morphology can expose more active sites. The calculated TOFs are shown in Fig. 5(d). The overpotentials of Ni$_3$S$_2$/NF, Cu$_2$S/Ni$_3$S$_2$/NF-2∼4 at TOF of 0.2 S^{-1} are 182, 168, 72, and 119 mV, respectively. In Fig. 6(a), TOFs denote that Cu$_2$S/Ni$_3$S$_2$/NF-3 has a higher catalytic activity.

Electrochemical Active Surface Area (ECSA) test was carried out. First, the CV curves were measured at various scan rate. Then, Half of the values of the positive and negative current density differences (Δj) at the median value of the scanning range are plotted versus the CV scanning rates in Fig. 5(f). The electrochemical double layer charge (C$_{dl}$) value can be obtained from the fit slope. Cu$_2$S/Ni$_3$S$_2$/NF-3 and Ni$_3$S$_2$/NF are both cut into 1 cm × 1 cm rectangles, with the same geometric surface area. The C$_{dl}$ of Cu$_2$S/Ni$_3$S$_2$/NF-3 (17.95 mF cm^{-2}) is

approximately 2.2 times that of Ni_3S_2/NF (8.23 mF cm^{-2}), indicating that the actual surface area of Cu_2S/Ni_3S_2/NF-3 is larger. From Fig. S4,† the surface loading of Cu_2S/Ni_3S_2 is 2.8 mg cm^{-2}.

The chronopotentiometry curve was measured to evaluate the mechanical strength and excellent mass transfer performance of Cu_2S/Ni_3S_2/NF-3. In Fig. 6(a), Cu_2S/Ni_3S_2/NF can maintain 95.1% activity stably for at least 58 hours. The fluctuation of the curve in the first 30 minutes is due to the gradual increase in the potential during the activation phase caused by the removal of the hydroxide/oxide on the electrode surface.[52] A CV was performed 2000 times continuously from 100 mV to −300 mV. In Fig. 6(b), the HER performance of Cu_2S/Ni_3S_2/NF-3 decreased slightly after the CV and need 70 mV to 10 mA cm^{-2}. Multistep chronopotentiometry (from 10 mA to 100 mA with 10 mA interval) was used to evaluate the mass transfer and stability of Cu_2S/Ni_3S_2/NF-3. The electrode reaction kinetics can be studied by EIS. The Nyquist diagrams of Cu_2S/Ni_3S_2/NF-2,3,4 were obtained at 200 mV. The equivalent circuit in Fig. 6(d): a constant-phase element (CPE) connected in parallel with a charge transfer resistance (R_{ct}), then an electrolyte resistance (R_s) is connected in series. The fitting line represented by the red line is semicircular, which means that the charge transfer controls the entire HER. R_{ct} can be determined in the semicircular low-frequency region to reflect the electron transport efficiency.[53] The R_{ct} values of Cu_2S/Ni_3S_2/NF-2,3,4 are 2.44 Ω, 0.79 Ω, and 1.98 Ω, respectively. Cu_2S/Ni_3S_2/NF-3 has the smallest R_{ct}, which means fast electron transfer. The excellent HER performance of Cu_2S/Ni_3S_2/NF-3 also echoes this result. By contrast, a small R_s value indicates that the bonding between the catalyst and the current collector is good.[54] The impedance results of Cu_2S/Ni_3S_2/NF-3 are consistent with the previous HER results, which can prove that it can be a candidate with excellent HER kinetics and outstanding electron transport performance.

4. Conclusion

Overall, the heterostructure Cu_2S/Ni_3S_2 were successfully synthesized by two-step hydrothermal method and exhibited excellent HER activity. Compared with the recently reported system, Cu_2S/Ni_3S_2/NF-3 has a lower overpotential ($\eta_{10} = 50$ mV). After vulcanization, the coral-like rough surface exposes more active sites. The heterostructure of Cu_2S/Ni_3S_2 exposes specific $\{\bar{2}10\}$ crystal planes as well as a large number of defects and (034) crystal planes, which helps expose more active sites. The structural characterization is consistent with the electrochemical test results. In HER process, Cu_2S/Ni_3S_2 interface increase the formation of S–H bonds, optimizing the adsorption capacity of S-doped sites for H. And Cu_2S promotes the transformation of the HER process into S-doped CuO. Therefore, the combination of Cu_2S and Ni_3S_2 further increases the catalytic activity.

Conflicts of interest

The authors declare no conflict of interest.

References

1 S. Chu, Y. Cui and N. Liu, The path towards sustainable energy, *Nat. Mater.*, 2017, **16**, 16–22, DOI: 10.1038/nmat4834.

2 Z. W. Seh, J. Kibsgaard, C. F. Dickens, I. B. Chorkendorff, J. K. Norskov and T. F. Jaramillo, Combining theory and experiment in electrocatalysis: insights into materials design, *Science*, 2017, **355**, 146, DOI: 10.1126/science.aad4998.

3 L. Peng, J. Shen, X. Zheng, R. Xiang, M. Deng, Z. Mao, Z. Feng, L. Zhang, L. Li and Z. Wei, Rationally design of monometallic NiO-Ni $_3$ S$_2$/NF heteronanosheets as bifunctional electrocatalysts for overall water splitting, *J. Catal.*, 2018, **369**, 345–351, DOI: 10.1016/j.jcat.2018.11.023.

4 K. Zeng and D. Zhang, Recent progress in alkaline water electrolysis for hydrogen production and applications, *Prog. Energy Combust. Sci.*, 2010, **36**, 307–326, DOI: 10.1016/j.pecs.2009.11.002.

5 M. Gong and H. Dai, A mini review of NiFe-based materials as highly active oxygen evolution reaction electrocatalysts, *J. Nano Res.*, 2015, **8**, 23–39, DOI: 10.1007/s12274-014-0591-z.

6 L. B. Lasia, Studies of the Hydrogen Evolution Reaction on Raney Nickel—Molybdenum Electrodes, *J. Appl. Electrochem.*, 2004, **34**, DOI: 10.1023/B:JACH.0000031161.26544.6a.

7 N. Danilovic, R. Subbaraman and D. Strmcnik, Enhancing the Alkaline Hydrogen Evolution Reaction Activity through the Bifunctionality of Ni(OH)$_2$/Metal Catalysts, *Angew. Chem.*, 2012, **124**, 12663–12666, DOI: 10.1002/anie.201204842.

8 C. Yang, M. Y. Gao, Q. B. Zhang, J. R. Zeng, X. T. Li and A. P. Abbott, *In situ* activation of self-supported 3D hierarchically porous Ni3S2 films grown on nanoporous copper as excellent pH-universal electrocatalysts for hydrogen evolution reaction, *Nano Energy*, 2017, **36**, 85–94, DOI: 10.1016/j.nanoen.2017.04.032.

9 X. F. A. B., Y. S. A., J. S. A., L. H. A. and Z. H. B., Superhydrophilic 3D peony flower-like Mo-doped Ni $_2$ S $_3$ @NiFe LDH heterostructure electrocatalyst for accelerating water splitting, *Int. J. Hydrogen Energy*, 2021, **46**, 5169–5180, DOI: 10.1016/j.ijhydene.2020.11.018.

10 J. J. Duan, Z. Han, R. L. Zhang, J. J. Feng and A. J. Wang, Iron, manganese co-doped Ni_3S_2 nanoflowers *in situ* assembled by ultrathin nanosheets as a robust electrocatalyst for oxygen evolution reaction, *J. Colloid Interface Sci.*, 2020, **588**, DOI: 10.1016/j.jcis.2020.12.062.

11 Q. Ma, C. Hu, K. Liu, S. F. Hung, D. Ou, H. Ming Chen, G. Fu and N. Zheng, Identifying the Electrocatalytic Sites of Nickel Disulfide in Alkaline Hydrogen Evolution Reaction, *Nano Energy*, 2017, **41**, 148–153, DOI: 10.1016/j.nanoen.2017.09.036.

12 Y. J. Liu, C. L. Luan, J. T. Yang, Y. Dong, Y. Wang, C. L. Qin, Z. Dong, S. Q. Wang, X. P. Dai and X. Zhang, In situ fabrication of dynamic self-optimizing Ni_3S_2 nanosheets as an efficient catalyst for the oxygen evolution reaction, *DTr*, 2019, **49**, 70–78, DOI: 10.1039/c9dt03885j.

13 M. R. Gao, J. X. Liang, Y. R. Zheng, Y. F. Xu, J. Jiang, Q. Gao, J. Li and S. H. Yu, An efficient molybdenum disulfide/cobalt diselenide hybrid catalyst for electrochemical hydrogen generation, *Nat. Commun.*, 2015, **6**, 5982, DOI: 10.1038/ncomms6982.

14 M. Tong, L. Wang, P. Yu, C. Tian, X. Liu, W. Zhou and H. Fu, Ni_3S_2 nanosheets *in situ* epitaxially grown on nanorods as high active and stable homojunction electrocatalyst for hydrogen evolution reaction, *ACS Sustainable Chem. Eng.*, 2017, **6**, 2474–2481, DOI: 10.1021/acssuschemeng.

15 X. Luo, P. Ji, P. Wang, R. Cheng and S. Mu, Interface Engineering of Hierarchical Branched Mo-Doped $Ni3S2$/$NixPy$ Hollow Heterostructure Nanorods for Efficient Overall Water Splitting, *Adv. Energy Mater.*, 2020, **10**, 1–11, DOI: 10.1002/aenm.201903891.

16 X. Liang, Y. Li, H. Fan, S. Deng and X. Xia, Bifunctional NiFe layered double hydroxide@Ni_3S_2 heterostructure as efficient electrocatalyst for overall water splitting, *Nanot*, 2019, **30**, 484001, DOI: 10.1088/1361-6528/ab3ce1.

17 J. Jian, L. Yuan, H. Qi, X. Sun, L. Zhang, H. Li, H. Yuan and S. Feng, Sn-$Ni3S2$ Ultrathin Nanosheets as Efficient Bifunctional Water Split-ting Catalyst with Large Current Density and Low Overpotential, *ACS Appl. Mater. Interfaces*, 2018, **10**, DOI: 10.1021/acsami.8b14603.

18 Y. Zhang, Y. Liu, M. Ma, X. Ren, Z. Liu, G. Du, A. M. Asiri and X. Sun, A Mn-doped $Ni2P$ nanosheet array: an efficient and durable hydrogen evolution reaction electrocatalyst in alkaline media, *Chem. Commun.*, 2017, **53**, 11048–11051, DOI: 10.1039/c7cc06278h.

19 G. Zhang, Y. S. Feng, W. T. Lu, D. He, C. Y. Wang, Y. K. Li, X. Y. Wang and F. F. Cao, Enhanced Catalysis of Electrochemical Overall Water Splitting in Alkaline Media by Fe Doping in $Ni3S2$ Nanosheet Arrays, *ACS Catal.*, 2018, **8**, 5431–5441, DOI: 10.1021/acscatal.8b00413.

20 N. Xie, D. D. Ma, X. T. Wu and Q. L. Zhu, Facile construction of self-supported Fe-doped $Ni3S2$ nanoparticle arrays for the ultralow-overpotential oxygen evolution reaction, *Nanoscale*, 2021, **13**, 1807–1812, DOI: 10.1039/d0nr07262a.

21 M. Wang, M. Zhang, W. Song, W. Zhong, X. Wang, J. Wang, T. Sun and Y. Tang, A highly stable $CoMo2S4$/$Ni3S2$ heterojunction electrocatalyst for efficient hydrogen evolution, *Chem. Commun.*, 2021, **57**, 785–788, DOI: 10.1039/d0cc06972h.

22 Q. Liu, L. Xie, Z. Liu, G. Du and X. Sun, A Zn-doped $Ni3S2$ nanosheet array as a high-performance electrochemical water oxidation catalyst in alkaline solution, *Chem. Commun.*, 2017, **53**, 12446–12449, DOI: 10.1039/c7cc06668f.

23 P. Phonsuksawang, P. Khajondetchairit, K. Ngamchuea, T. Butburee and T. Siritanon, Enhancing performance of $NiCo2S4$/$Ni3S2$ supercapacitor electrode by Mn doping, *Electrochim. Acta*, 2020, **368**, 137634, DOI: 10.1016/j.electacta.2020.137634.

24 Q. Zhang, N. Liu and J. Guan, Accelerative oxygen evolution by Cu-doping into Fe-Co oxides, *Sustainable Energy Fuels*, 2020, **4**, 143–148, DOI: 10.1039/c9se00928k.

25 Z. Guo, X. Wang, Y. Gao and Z. Liu, Co/Cu-modified NiO film grown on nickel foam as a highly active and stable electrocatalyst for overall water splitting, *DTr*, 2020, **49**, 1776–1784, DOI: 10.1039/c9dt04771a.

26 X. Du, Y. Ding and X. Zhang, Cu-doped $Ni3S2$ interlaced nanosheet arrays as high-efficiency electrocatalyst boosting the alkaline hydrogen evolution, *ChemCatChem*, 2021, 1824–1833, DOI: 10.1002/cctc.202001838.

27 S. Chu, W. Chen, G. Chen, J. Huang, R. Zhang, C. Song, X. Wang, C. Li and K. Ostrikov, Holey Ni-Cu phosphide nanosheets as a highly efficient and stable electrocatalyst for hydrogen evolution, *Appl. Catal., B*, 2018, **243**, 537–545, DOI: 10.1016/j.apcatb.2018.10.063.

28 Y. Jiao, W. Hong, P. Li, L. Wang and G. Chen, Metal-Organic Framework Derived Ni/NiO Micro-particles with Subtle Lattice Distortions for High-performance Electrocatalyst and Supercapacitor, *Appl. Catal., B*, 2018, **244**, 732–739, DOI: 10.1016/j.apcatb.2018.11.035.

29 A. P. Murthy, J. Theerthagiri, K. Premnath, J. Madhavan and K. Murugan, Single-Step Electrodeposited Molybdenum Incorporated Nickel Sulfide Thin Films from Low-Cost Precursors as Highly Efficient Hydrogen Evolution Electrocatalysts in Acid Medium, *J. Phys. Chem. A*, 2017, **121**, 11108–11116, DOI: 10.1021/acs.jpcc.7b02088.

30 X. B. Wang, J. J. Hu, W. D. Liu, G. Y. Wang, J. An and J. S. Lian, Ni–Zn binary system hydroxide, oxide and sulfide materials: synthesis and high supercapacitor performance, *J. Mater. Chem. A*, 2015, **3**, 23333–23344, DOI: 10.1039/c5ta07169k.

31 Y. Zhu, H. D. Yang, K. Lan, K. Lqbal, Y. Liu, P. Ma, Z. M. Zhao, S. Luo, Y. T. LUO and J. T. Ma, Optimization of iron-doped $Ni3S2$ nanosheets by disorder engineering for oxygen evolution reaction, *Nanoscale*, 2019, **11**, 2355–2365, DOI: 10.1039/c8nr08469f.

32 A. H. Jayatissa and G. Sumanasekera, Surface and gas sensing properties of nanocrystalline nickel oxide thin films, *Appl. Surf. Sci.*, 2013, **276**, 291–297, DOI: 10.1016/j.apsusc.2013.03.085.

33 M. C. Biesinger, B. P. Payne, L. W. M. Lau, A. Gerson and R. S. C. Smart, X-ray photoelectron spectroscopic chemical state quantification of mixed nickel metal, oxide and hydroxide systems, *Surf. Interface Anal.*, 2009, **41**, 324–332, DOI: 10.1002/sia.3026.

34 X. Xun, H. Liu, Y. Su, J. Zhang, J. Niu, H. Zhao, G. Zhao, Y. Liu and G. Li, One-pot synthesis Ni-Cu sulfide on Ni foam with novel three-dimensional prisms/spheres hierarchical structure for high-performance supercapacitors, *J. Solid State Chem.*, 2019, **275**, 95–102, DOI: 10.1016/j.jssc.2019.04.012.

35 Y. Li, L. Cao, L. Qiao, M. Zhou, Y. Yang, P. Xiao and Y. Zhang, Ni–Co sulfide nanowires on nickel foam with ultrahigh capacitance for asymmetric supercapacitors, *J. Mater. Chem. A*, 2014, **2**, 6540–6548, DOI: 10.1039/c3ta15373h.

36 Y. G. Lin, Y. K. Hsu, C. J. Chuang, Y. C. Lin and Y. C. Chen, Thermally activated Cu/Cu2S/ZnO nanoarchitectures with surface-plasmon-enhanced Raman scattering, *J. Colloid Interface Sci.*, 2015, **464**, 66–72, DOI: 10.1016/j.jcis.2015.10.043.

37 S. Li, C. Xi, Y. Jin, D. Wu and X. W. Du, Ir-O-V Catalytic Group in Ir-Doped NiV(OH)2 for Overall Water Splitting, *ACS Energy Lett.*, 2019, **4**, 1823–8195, DOI: 10.1021/acsenergylett.9b01252.

38 Y. Liu, Q. Li, R. Si, G. D. Li, W. Li, D. P. Liu, D. Wang, L. Sun, Y. Zhang and X. Zou, Coupling Sub-Nanometric Copper Clusters with Quasi-Amorphous Cobalt Sulfide Yields Efficient and Robust Electrocatalysts for Water Splitting Reaction, *Adv. Mater.*, 2017, **29**, 1606200, DOI: 10.1002/adma.201606200.

39 J. X. Feng, J. Q. Wu, Y. X. Tong and G. R. Li, Correction to Efficient Hydrogen Evolution on Cu Nanodots-Decorated Ni 3 S 2 Nanotubes by Optimizing Atomic Hydrogen Adsorption and Desorption, *J. Am. Chem. Soc.*, 2020, **142**, 18997, DOI: 10.1021/jacs.9b06861.

40 Z. Zang, X. Wang, X. Li, Q. Zhao and Z. Lu, Co 9 S 8 Nanosheet Coupled Cu 2 S Nanorod Heterostructure as Efficient Catalyst for Overall Water Splitting, *ACS Appl. Mater. Interfaces*, 2021, **13**, DOI: 10.1021/acsami.0c20820.

41 L. L. Feng, G. Yu, Y. Wu, G. D. Li, L. Hui, Y. Sun, T. Asefa, W. Chen and X. Zou, High-Index Faceted Ni3S2 Nanosheet Arrays as Highly Active and Ultrastable Electrocatalysts for Water Splitting, *J. Am. Chem. Soc.*, 2015, **137**, 14023–14026, DOI: 10.1021/jacs.5b08186.

42 X. Zhang, Y. Zhao, Y. Zhao, R. Shi, G. Waterhouse and T. Zhang, A Simple Synthetic Strategy toward Defect-Rich Porous Monolayer NiFe-Layered Double Hydroxide Nanosheets for Efficient Electrocatalytic Water Oxidation, *Adv. Energy Mater.*, 2019, **9**, 1–7, DOI: 10.1002/aenm.201900881.

43 K. B. Keun, K. Soo-Kil, C. S. Ki and K. J. Jeong, Enhanced Catalytic Activity of Electrodeposited Ni-Cu-P toward Oxygen Evolution Reaction, *Appl. Catal., B*, 2018, **237**, 409–415, DOI: 10.1016/j.apcatb.2018.05.082.

44 Y. Yang, H. Mao, R. Ning, X. Zhao and W. Cai, Ar Plasma-assisted P-doped Ni3S2 with S Vacancies for efficient electrocatalytic water splitting, *DTr*, 2021, **50**, 2007–2013, DOI: 10.1039/d0dt03711g.

45 H. Xu, Y. Liao, Z. Gao, Y. Qing, Y. Wu and L. Xia, A branch-like Mo-doped Ni3S2 nanoforest as a high-efficiency and durable catalyst for overall urea electrolysis, *J. Mater. Chem. A*, 2021, **9**, 3418–3426, DOI: 10.1039/d0ta09423d.

46 D. Yang, L. Cao, L. Feng, J. Huang and J. Wang, Controlled Synthesis of V-Doped Heterogeneous Ni3S2/NiS Nanorod Arrays as Efficient Hydrogen Evolution Electrocatalysts, *Langmuir*, 2020, **37**, DOI: 10.1021/acs.langmuir.0c02943.

47 W. J. Dai, K. Ren, Y. A. Zhu, Y. Pan, J. Yu and T. Lu, Flower-like CoNi2S4/Ni3S2 nanosheet clusters on nickel foam as bifunctional electrocatalyst for overall water splitting, *J. Alloys Compd.*, 2020, **844**, 156252, DOI: 10.1016/j.jallcom.2020.156252.

48 Y. Wu and H. He, Electrodeposited nickel–iron–carbon–molybdenum film as efficient bifunctional electrocatalyst for overall water splitting in alkaline solution, *Int. J. Hydrogen Energy*, 2018, **44**, 1336–1344, DOI: 10.1016/j.ijhydene.2018.11.168.

49 T. T. Chen, R. Wang, L. K. Li, Z. J. Li and S. Q. Zang, MOF-derived Co9S8/MoS2 embedded in tri-doped carbon hybrids for efficient electrocatalytic hydrogen evolution, *J. Energy Chem.*, 2019, **44**, 90–96, DOI: 10.1016/j.jechem.2019.09.018.

50 R. Nivetha and A. N. Grace, Manganese and zinc ferrite based graphene nanocomposites for electrochemical hydrogen evolution reaction, *J. Alloys Compd.*, 2019, **796**, 185–195, DOI: 10.1016/j.jallcom.2019.05.021.

51 Y. S. Park, W.-S. Choi, M. J. Jang, J. H. Lee, S. Park, H. Jin, M. H. Seo, K.-H. Lee, Y. Yin, Y. Kim, J. Yang and S. M. Choi, Three-Dimensional Dendritic Cu–Co–P Electrode by One-Step Electrodeposition on a Hydrogen Bubble Template for Hydrogen Evolution Reaction, *ACS Sustainable Chem. Eng.*, 2019, **7**, 10734–10741, DOI: 10.1021/acssuschemeng.9b01426.

52 K. Zhang, W. Xiao, J. Li, J. Liu and C. Yan, Two-step Preparation of Porous Nickel-sulfur Electrode for Hydrogen Evolution in Alkaline Water Electrolysis, *Electrochim. Acta*, 2017, **228**, 422–427, DOI: 10.1016/j.electacta.2017.01.105.

53 Y. Niu, X. Qian, C. Xu, H. Liu, W. Wu and L. Hou, Cu-Ni-CoSex quaternary porous nanocubes as enhanced Pt-free electrocatalysts for highly efficient dye-sensitized solar cells and hydrogen evolution in alkaline medium, *Chem. Eng. J.*, 2019, **357**, 11–20, DOI: 10.1016/j.cej.2018.09.116.

54 Y. Tian, J. Yu, H. Zhang, C. Wang, M. Zhang, Z. Lin and J. Wang, 3D porous Ni-Co-P nanosheets on carbon fiber cloth for efficient hydrogen evolution reaction, *Electrochim. Acta*, 2019, **300**, 217–224, DOI: 10.1016/j.electacta.2019.01.101.